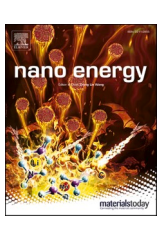


Contents lists available at ScienceDirect

## Nano Energy

journal homepage: www.elsevier.com/locate/nanoen





# Dual-pace transient heat conduction in vertically aligned carbon nanotube arrays induced by structure separation

Yangsu Xie<sup>a</sup>, Hamidreza Zobeiri<sup>b</sup>, Liping Xiang<sup>a</sup>, Gyula Eres<sup>c,\*</sup>, Jianmei Wang<sup>d,\*</sup>, Xinwei Wang<sup>b,\*</sup>

- <sup>a</sup> College of Chemistry and Environmental Engineering, Shenzhen University, Shenzhen 518055, Guangdong, China
- b Department of Mechanical Engineering, 271 Applied Science Complex II, Iowa State University, Ames, IA 50011, USA
- <sup>c</sup> Oak Ridge National Laboratory, Materials Science and Technology Division, Bldg 4100, MS 6118, Oak Ridge, TN 37831, USA
- <sup>d</sup> School of Power and Mechanical Engineering, Wuhan University, Wuhan 430072, China

#### ARTICLE INFO

#### Keywords: vertically aligned carbon nanotubes dual-pace transient thermal response cryogenic state coiled morphology parallel heat transfer

#### ABSTRACT

Vertically aligned arrays of carbon nanotubes (CNTs) are attractive for a wide range of macroscopic applications which can exploit the remarkable properties of individual nanotubes. In this work, an abnormal behavior of CNT bundles in heat conduction is discovered under the transient electro-thermal characterization. The measured voltage change over the sample shows a dual-pace thermal response (DTR), which could not be fitted using a single thermal diffusivity heat transfer model. Instead, two thermal diffusivities are determined from the DTR phenomenon. Three rounds of cryogenic experiments are conducted to investigate the physics behind DTR phenomenon. It starts to emerge when the temperature is reduced to a certain level. After two rounds of cryogenic experiments, the DTR phenomenon becomes permanent from 295 K to 10 K. The nano-scale structure separation induced by the increased thermal strain leads to macroscale structure separation, which results in two parallel heat conduction paths responsible for the DTR phenomenon. By building a new parallel heat transfer model taking both the transient and steady-state electrical and thermal response into consideration, the area ratio of separated CNTs is determined. This result uncovers the existence of coiled morphology and nano-structure evolution of CNTs under cryogenic state and its effect on thermal and electrical transport, especially on their transient behaviors. Knowledge of the thermal transport in these CNTs arrays is important considering the fact that transient thermal response strongly affects their mechanical, optical, and electrical behaviors.

#### 1. Introduction

Vertically aligned arrays of carbon nanotubes (VACNTs) are attractive for a wide range of macroscopic applications which can exploit the remarkable properties of individual CNTs [1]. Application of VACNTs in thermal interface management [2–4], thermionic and field-emission electron sources [5], strain and temperature sensors [6], loudspeakers [7,8], incandescent displays [9], energy conversion [10] and storage [11], etc. have been widely reported. Thermal chemical vapor deposition (CVD) is a technique capable of directly producing vertically aligned arrays of CNTs on various substrates [12–14], which uses thermal energy to promote the reaction between the carbon source and the catalyst at high temperature by thermal decomposition. In terms of the theoretical limits of electrical and thermal conductivities for individual CNTs, alignment of CNTs is an important factor. However, in most cases,

CNTs are not perfectly aligned in VACNTs [15], where helical and zigzag morphology are usually observed. Wang et al. investigated the evolution of straight tubes and coiled tubes during CVD process and found that the coiled morphologies were driven by the competing factors of collective growth and spatial constraints [16]. Due to their helical morphology, helical CNT bundles exhibit different physical properties, such as superelasticity, high specific strength, chirality, and electromagnetic cross-polarization characteristics [17], which bring them advantages in applications such as field emission [18], microwave absorbing [19], and strain sensor [20]. Knowledge of thermal transport in these micro/nanoscale structures has become indispensable considering the temperature and thermal response of materials strongly affect their mechanical, optical, and electrical properties.

The random alignment and curvatures of CNTs provide significant phonon and electron scattering sites. Furthermore, the effect of thermal

E-mail addresses: eresg@ornl.gov (G. Eres), jmwang@whu.edu.cn (J. Wang), xwang3@iastate.edu (X. Wang).

<sup>\*</sup> Corresponding authors.

contact resistance is also significant in CNTs network [21-24]. As a result, the thermal conductivity (k) of VACNTs arrays is much lower than the intrinsic k of CNTs. The transient electro-thermal (TET) technique [25,26], thermal bridge [27], 30 method [28], laser-flash [29], and Raman method etc. [30-33] have been used for thermal characterization of CNTs materials. Bauer et al. measured k of vertically aligned CNT arrays to be only 49–79 W m<sup>-1</sup> K<sup>-1</sup> [34]. Other works reported even lower values (<25 W m<sup>-1</sup> K<sup>-1</sup>) [35,36]. k of MWCNT films were reported to be about 15 W m<sup>-1</sup> K<sup>-1</sup> by using the photothermal reflectance technique.[37]. For SWCNTs mats, k was measured to be about 35 W m<sup>-1</sup> K<sup>-1</sup> according to Hone et al. [38] To study the effect of thermal contact resistance, T-type method [39], micro-heater/sensor method [40], as well as laser-flash Raman mapping method [41] have been used for characterizing the thermal contact resistance between individual carbon tubes. In addition, it should be noted that the porosity level and density of CNT samples also cause differences in k. The density of a disk-shape MWCNT fabricated by spark plasma sintering (SPS) from 800 to 2000 °C were from 350 to 1450 kg m<sup>-3</sup> [42]. The apparent densities of randomly aligned multi-walled CNTs buck papers were calculated at 459 and 543 kg  $\mathrm{m}^{-3}$  [30]; while for MWCNTs bundles, it was reported to be 116–234 kg m<sup>-3</sup> [35]. By taking the porosity effect into consideration, Xie et al. reported the intrinsic k of CNT walls in CNTs bundles to be as high as 754 W m<sup>-1</sup> K<sup>-1</sup> after the thermal annealing treatment [26].

Compared with thermal conductivity, thermal diffusivity tells more about the CNT-CNT contact effect and curvature effect since it is less affected by the porosity level. Guo et al. found that the curvature morphology reduced the thermal diffusivity ( $\alpha$ ) of multiwalled CNT bundles by 10 folds by elongating the heat propagation route from first order estimation based on the alignment [43]. Xie et al. calculated the intrinsic k of CNT walls from the heat transfer path aspect, where the 3D ratio of the curvature length of CNTs over the straight-line length was estimated [26]. Deng et al. studied the thermal diffusivity and conductivity of carbon nanocoils from 290 to 10 K and uncovered a correlation between  $\alpha$  and the line diameter [44]. To have a better understanding of phonon scattering mechanisms, the temperature-dependent thermal reffusivity (the reciprocal of thermal diffusivity) has been proposed and studied[45]. It is an intrinsic property of materials which can be used to directly characterize the phonon transfer resistivity. It was found that as temperature goes down, the thermal reffusivity of normal carbon materials including graphite, graphene foam, and carbon nanocoils decreased and finally reached a residual value at the 0 K limit, whose value was dependent on the structural domain size of materials [45–48]. However, for composite materials such as the VACNTs arrays, where large amount of inter-tube contacts exist, the behavior of the phonon scattering can be more complex. In addition, due to the existence of both straight and coiled morphologies of CNTs, the interplay of the two morphologies is expected to be responsible for macroscopic thermal and electrical behaviors [49,50].

In this work, an abnormal thermal behavior of CNT bundles in heat conduction is discovered by using the TET technique. Upon step DC current heating, the sample experiences a first fast resistance decay and then a slow one, meaning dual-pace thermal response (DTR). Contrast to normal sample's exponential variation with a single time constant, DTR cannot be simply interpreted by normal transient heat conduction. This phenomenon is impossible to observe in other heat conduction studies, especially studies using the steady state method. To uncover the physics of DTR, three rounds of cryogenic experiments are conducted to investigate the thermal diffusivity, thermal conductivity, and specific heat from 295 K to 10 K. The unique structure of the CNT bundles constitutes parallel distinct thermal transport paths which result in DTR. A new parallel heat transfer model is developed to interpret the observed DTR phenomenon by taking both the transient and steady state electrical and thermal response into consideration based on the micro-structure evolution of VACNT arrays.

#### 2. Material synthesis and structure characterization

The VACNTs is grown by chemical vapor deposition (CVD) on a Si 100 wafer using a two-layer metal catalyst film consisting of 10 nm of Al and 1 nm of Fe. The experimental details can be found in the literature [51]. Briefly, the catalyst film is deposited on a Si wafer using electron beam evaporation through a shadow mask with periodic holes of 200  $\mu m$  diameter. Acetylene is used as the carbon source gas, which is flowed concurrently with ferrocene sublimated from a thermal source in the CVD process. After that, a vertically aligned array sample of 4.5 mm thickness is obtained. The resulting CNTs are aligned vertically and formed into bundles by Van der Waals forces, where continuous CNT bundles can be easily drawn from the VACNTs. MWCNT bundles with a diameter of about 200  $\mu m$  are then harvested from the array for the subsequent thermal transport study.

The micro-structure of the as-prepared CNT bundles is observed under scanning electron microscope (SEM). As shown in Fig. 1a, a good alignment along the axial direction under low magnification can be observed. However, the coexistence of two morphologies of CNTs, one being relatively straight whereas the other taking regularly coiled morphology, is also evident under higher magnifications (Fig. 1b). These morphologies are resulted from the competing effects of collective growth and spatial constraints during the CVD process [16]. Fig. 1c is a transmission electron microscopy (TEM) image of a MWCNT in the bundle, which reveals that the CNT bundles consist of MWCNTs with typical outer diameter from 18 to 25 nm. The wall thickness ranges from 15 to 22 layers. X-ray diffraction (XRD) was performed to study the crystallite structure of the CNT bundles. As presented in Fig. 1d, three peaks are observed in the XRD profile. The strong and sharp (002) peak at around 25.8° corresponds to the inter-planar spacing of 0.34 nm, which is very close to 0.335 nm for pure graphite. This result indicates that the inter-wall impurities are rare. The other two small diffraction peaks at  $42.8^{\circ}$  and  $53.4^{\circ}$  correspond to the (100) and (004) reflections.

In order to investigate the orientation distribution of CNTs inside the bundle, a polarized Raman experiment is performed. Fig. 1e shows one of the Raman spectrum of the CNTs bundles. Fig. 1f shows the CNT bundle and polarization direction of the continuous wave (CW) laser. Here,  $\theta_L$  is the polarization angle, and  $\alpha_L$  represents the orientation of each nanotube inside the bundle. It has been proved that the light polarization-dependent absorption of CNT is proportional to  $\cos^2(\theta_L - \alpha_L)$  [52], which shows that the light absorption by a nanotube reaches maximum when it is parallel to the light polarization direction. Knowing that Raman intensity is higher when the light absorption is higher, using the light absorption relationship with polarization and individual nanotube's orientation, the orientation distribution function  $g(\alpha_L)$  of CNTs inside the bundle affects the polarized Raman intensity as

$$f(\theta_L) = \int_{\rho^{\circ}}^{360^{\circ}} g(\alpha_L) \cos^2(\theta_L - \alpha_L) d\alpha_L, \tag{1}$$

where  $f(\theta_L)$  is directly proportional to the Raman intensity at angle  $\theta_L$ . Function  $g(\alpha_L)$  represents the probability of finding nanotubes at different direction  $\alpha_L$  with respect to the bundle's axial direction. Here, using the polarized Raman experiment, we can find the polarized Raman intensity of G peak of CNT bundle against  $\theta_L$ .

Fig. 1g shows the polar contour of Raman spectra of CNT bundle in the range of 1400–1750 cm<sup>-1</sup> under 532 nm CW laser irradiation. The Raman intensity of G peak against  $\theta_L$  is indicated in the figure. The Raman intensity of the G peak is maximum near  $0^\circ$  and  $180^\circ$ . The intensity of G peak is normalized by the Raman intensity of G peak of high purity graphene paper to discard the effects of beam splitter and other optical components of the Raman system [53]. The normalized Raman intensity of the G peak is fitted by Eq. (1) to find the orientation distribution  $g(\alpha_L)$  of CNTs. The fitted  $g(\alpha_L)$  function is plotted in Fig. 1h. As shown in this figure, the probability of finding CNTs aligned with the bundle's axial direction reaches the maximum at  $0^\circ$  and  $180^\circ$ . This value

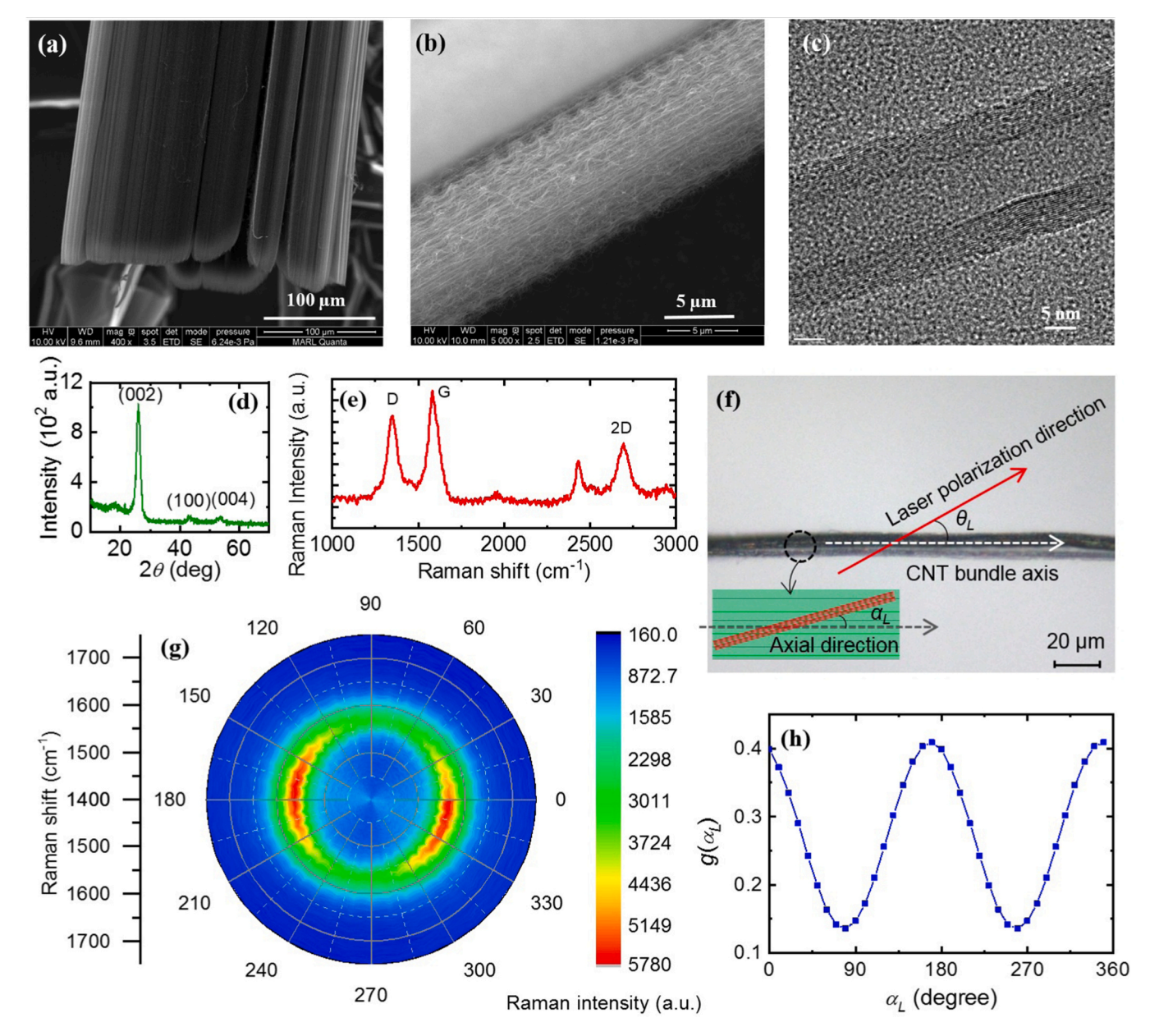


Fig. 1. (a)-(b) SEM images of the CNT bundles under different magnifications. (c) The TEM image of CNT in the bundle. (d) The XRD spectrum. (e) One of the Raman spectrum of CNT bundles. (f) The schematic of the polarized Raman experiment. (g) The polar contour of Raman signals against  $\theta_L$  in the range of 1400–1750 cm<sup>-1</sup> under 532 nm CW laser irradiation. (h) The normalized function  $g(\alpha_L)$  against the orientation angle.

is two times higher than the minimum probability, which happens at  $90^\circ$  and  $270^\circ.$  This sine-wave-like alignment distribution shows that although the majority of the nanotubes are aligned along the bundle's axial direction, a significant amount of them are also aligned in other directions.

## 3. DTR phenomenon discovered in TET characterization

### 3.1. Physics of TET characterization

The DTR phenomenon is discovered during the thermal diffusivity ( $\alpha$ ) measurement of CNT bundles by using the transient electrothermal (TET) technique (Fig. 2a). The TET technique features strong signal level and fast measurement, and can be applied to metallic, semi-conductive and nonconductive materials [47,54–57]. The measurement accuracy of this technique has been extensively examined by characterizing known materials, including both metallic and dielectric materials with

measurement uncertainty better than  $\pm 10\%$  [47,54–57]. In the experiment, the sample is suspended between two gold coated silicon electrodes on a glass wafer and connected by using a small amount of silver paste. Fig. 2b shows a microscopy image of the suspended CNT bundle sample. The sample is then placed in a vacuum chamber, where the vacuum level is maintained below 0.5 mTorr. Due to the low air pressure in the chamber, the heat convection by air can be neglected.

Fig. 2a shows the schematic of the experimental set-up. During TET measurement, a small step current is fed through the sample by a current source to induce fast joule heating, which leads to a fast temperature rise. The corresponding voltage-time profiles (V-t) are collected by using an oscilloscope. In general, the higher  $\alpha$  of the sample, the faster temperature evolution and shorter time to reach the steady state. The transient temperature change can be used to determine  $\alpha$  of the to-be-measured sample. During this transient process, the heat transfer in the sample can be treated one-dimensional with sound accuracy. The governing equation is expressed as [54,58].

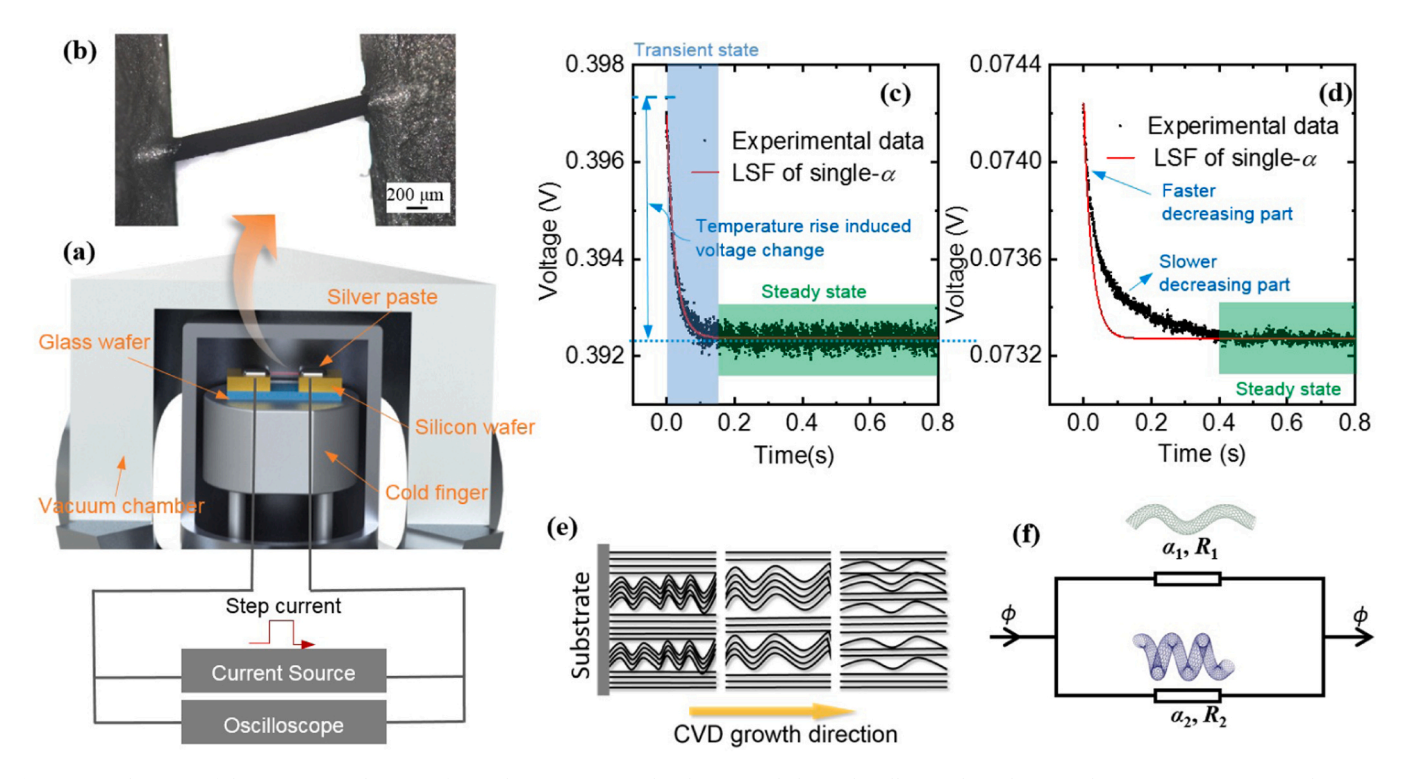


**Fig. 2.** (a) Schematic of the experimental set-up of TET characterization. (b) The suspended CNT bundle sample under optical microscope. (c) A typical V-t curve from the TET measurement of the sample at 295 K in the first round of cryogenic experiment. It can be fitted by LSF based on the single- $\alpha$  model in Eq. (4) with sound accuracy. (d) One of the V-t curve where the DTR phenomenon emerges. It cannot be fitted by LSF based on the single- $\alpha$  model in Eq. (4) for the entire curve. (e) A schematic of the macroscopic CNT morphologies where some of the initially straight CNTs develop coiled morphologies due to the competing factors of collective growth and spatial constraints [16]. (f) A schematic showing the parallel heat transfer model in the VACNTs arrays.

$$\frac{1}{\alpha} \frac{\partial \theta(x,t)}{\partial t} = \frac{\partial^2 \theta(x,t)}{\partial x^2} + \frac{I^2 R}{k L A_c} + \frac{Q_{rad}}{k L A_c}.$$
 (2)

In this equation,  $\theta = T - T_0$  is the temperature rise of the sample (T: temperature,  $T_0$ : initial temperature),  $\alpha$  is the thermal diffusivity, t is time, L and  $A_c$  are the suspended length and the cross-sectional area of the sample, respectively, I is the current passing through the sample, R the resistance of the sample, and  $Q_{\rm rad}$  the heat transfer rate of radiation from the sample surface. The solution to the partial differential equation can be obtained by integral of Green's function, which is:

$$G_{XII}\left(x,t/x',\tau\right) = \frac{2}{L} \sum_{m=1}^{\infty} \exp\left[-m^2 \pi^2 \alpha (t-\tau)/L^2\right] \times \sin\left(m\pi \frac{x}{L}\right) \sin\left(m\pi \frac{x'}{L}\right)$$
(3)

The temperature distribution along the sample is expressed as  $T(x,t) = T_0 + \alpha/k \cdot \int_{\tau=0}^t \int_{x'=0}^L q_0 G_{XII} dx' d\tau$ , where  $\alpha$ , cp, and k are the density, specific heat, and thermal conductivity of the sample, respectively [54, 58]. The steady-state heat transfer governing equation is:  $k\partial^2 T/\partial x^2 + q_0 = 0$ . Here, k is the thermal conductivity and  $q_0$  is the joule heating rate per unit volume. The temperature distribution along the sample can be expressed as  $T(x) = T_0 - q_0(x^2 - xL)/(2k)$ , where x is the position along the axial direction and L is the sample length. The temperature is the maximum at the center point, while stays at room temperature  $T_0$  at the two electrodes.

The normalized temperature rise for the transient state, which is defined as  $T^* = [T(t) - T_0]/[T(t \rightarrow \infty) - T_0]$ , can be derived as [54]:

$$T^* \cong \frac{48}{\pi^4} \sum_{m=1}^{\infty} \frac{1 - (-1)^m}{m^2} \frac{1 - \exp[-m^2 \pi^2 \alpha_m t / L^2]}{m^2}.$$
 (4)

Note this normalized temperature rise can also be simplified as  $T^* =$ 

 $1-0.99e^{-9.911\times\alpha_mt/t^2}$  [59]. The small current used for the TET measurement (around 50 mA) induces only a small temperature rise, within which the temperature coefficient of resistance can be assumed constant. Thus,  $T^*$  can be obtained by the normalized V-t curve. Fig. 2c shows a typical V-t curve of the CNT bundle sample obtained at 295 K in the first round of cryogenic experiment, where the signal can be divided into two parts: the transient state and the steady state. This is a normal TET signal for materials with negative temperature coefficient of resistance. Upon the step current heating, the V-t curve presents a fast decreasing behavior due to the joule heating. Then the temperature reaches a steady state, resulting from the energy balance of joule heating, heat conduction and thermal radiation. The normal V-t curve can be very well fitted by using the least square fitting (LSF) method based on Eq. (4) [54] as shown in Fig. 2c. The trial  $\alpha$  value which gives the best fit of the experiment data is taken as the sample's  $\alpha$ .

In the experiment, we used silver paste to connect the sample with gold-coated silicon electrodes. The particle size of the silver paste is much smaller than that of the bundle, which makes the electrical and thermal contact resistance negligible. In our previous work, the thermal diffusivity of silver paste connected samples with high electrical and thermal conductivity (electrical resistance less than  $2\,\Omega$  and thermal conductivity of hundreds of W m<sup>-1</sup> K<sup>-1</sup>) have been measured by using the TET technique, including platinum wires and high purity graphene films. Sound agreement was obtained between the measured thermal diffusivity and reference values, which indicated that the thermal contact resistance is negligible [54]. In addition, for the high purity graphene film samples, it was found that the connection by silver paste results in only less than  $0.2 \Omega$  contact resistance [59]. The contacting method for our CNT bundles is similar to that for the high purity graphene film. Moreover, the thermal contact resistivity between a high- $T_c$ superconductor and a copper block connected by silver paste is quite stable at around 10<sup>2</sup> mm<sup>2</sup> K/W above 40 K [60]. If the contacting area between the sample and silver paste is  $0.2 \text{ mm} \times 0.5 \text{ mm} \times 4$ , the thermal contact resistance at two ends of the sample can be estimated as 250 K/W. For comparison, the thermal resistance of the CNT bundle sample is calculated to be about  $9.37\times10^3$  K/W at RT. Thus, the thermal contact resistance takes less than 2.7% of the thermal resistance of the sample if calculated from Fujishiro et al.'s experimental report.

In our TET measurement, the thermal radiation effect is always evaluated with great care to ensure validity of the measurement data. The thermal radiation effect with the surrounding environment contributes insignificantly in the determined thermal diffusivity/ conductivity (calculated to be less than 2%). The measured thermal diffusivity and conductivity consists of two parts, which includes the real thermal diffusivity/conductivity and the thermal radiation with surrounding environment as:  $k_m = k_{real} + 16\varepsilon_r \sigma T_0^3 l^2/(\pi^2 D)$  [47,61]. In TET measurement, since the temperature increase is quite small ( $\Delta T \ll T$ ) and the sample's aspect ratio is very large, the radiation effect contributes insignificantly in the determined thermal diffusivity/conductivity (calculated to be less than 2%). Therefore, the error from the thermal radiation with environment is insignificant on the final result. In addition, for the thermal radiation between the carbon nanotubes, the effect is even smaller. The reason is the very small temperature difference between the carbon nanotubes. Thus, the effect of thermal radiation between the carbon nanotubes is negligible.

## 3.2. Discovery of DTR phenomenon and temperature's effect

The DTR phenomenon is first discovered during the cryogenic TET characterization and it only emerges at certain temperatures. To study the thermal properties of CNT bundles at cryogenic temperatures, the sample is put on a cold head in a vacuum chamber (Janis, closed cycle refrigerator system) where the temperature is controlled to vary from 295 K to 10 K. As shown in Fig. 2a, the electrode base with the sample is placed on the cold finger of the system. The cold finger is covered by a radiation shield to block the thermal radiation from environment. A heater and thermometer are installed on the cold finger to precisely control the sample temperature through a temperature controller. The temperature points and the cooling/heating rate are set as the same for the three rounds of experiments. The TET experiments are conducted after the temperature of the cold finger reaches the desired temperature. During the TET characterization, the temperature of the cold finger is controlled to be constant.

The TET characterization is conducted every 5–30 K. As temperature goes down to 35 K, we observe a DTR phenomenon. Fig. 2d shows one of the DTR signals. It can be seen that the V- t curve shows a fast decreasing pattern just like that in Fig. 2c at the beginning. However, there is an extra slower-decreasing part emerging after the fast-decreasing part. As shown in the figure, this abnormal DTR V- t curves cannot be fitted by the LSF based on the model described by Eq. (4), which indicates that the heat transfer process in these situations are more complex than the model presented in Eq. (4). As will be discussed later, these abnormal processes have nothing to do with electrical inductance or capacitance effect as their magnitude is proportional to the joule heating power, not the electrical current level.

As illustrated in the structure characterization section, two distinctly different CNT morphologies developed in the CNTs arrays. One morphology is relatively straight tubes, while the other is coiled tubes. Fig. 2e shows a schematic of the root growth mechanism illustrating that some of the initially straight CNTs develop into coiled morphologies in latter stages of growth during CVD process. Based on the structure characteristics and the observed TET signals, we speculate that the observed DTR phenomenon is resulted from two parallel routes of heat conduction in the CNT bundles where the straight and coiled CNTs constitute two parallel heat transport paths for phonons. As illustrated in Fig. 2f, when heat is conducted from the middle point of the sample to the end, two parallel heat paths are available.  $\alpha_1$  and  $\alpha_2$  correspond to the thermal diffusivity of the straight tubes and the coiled tubes, respectively.  $R_1$  and  $R_2$  are the corresponding electrical resistance of the

two structures, respectively. As shown in Eq. (4), for the one-dimensional heat transfer model, the speed of the temperature rise is dependent on the thermal diffusivity  $\alpha$  and the suspended length l as  $\alpha/l^2$ . The real heat transfer length of the straight CNTs is shorter than that of the coiled CNTs. Therefore, since the thermal diffusivity of the CNTs can be assumed the same, the straight CNTs show a faster but lower temperature rise; while the coiled ones show a slower but higher temperature rise. Below we show how to use this two-pace parallel heat conduction model to fit the experimental data.

In our first round cryogenic experiment, it is discovered that the DTR phenomenon starts to emerge when the temperature is reduced to a certain level. To illustrate this, the normalized temperature rise profiles obtained bv the normalized voltage  $T^* = [V(t) - V_0]/[V(t \rightarrow \infty) - V_0]$  at selected temperatures are presented in Fig. 3a with offset for comparison. The  $T^*$ -t profiles present a normal single-stage temperature increasing pattern at the temperature range of 295-55 K. When the temperature is lowered down to 35 K, they begin to show a DTR pattern: a fast-increasing stage and a slow-increasing stage. The slow-increasing pattern continues to develop in TET when the temperature is further lowered down to 10 K. This DTR pattern cannot be fitted using the TET model as presented in Eq. (4). Instead, a dual- $\alpha$ physical model can be used to fit the DTR data [59]:

$$T^* = Ae^{-9.911 \times \alpha_1 t/L^2} + Ce^{-9.911 \times \alpha_2 t/L^2} + B.$$
 (5)

In this model,  $\alpha_1$  and  $\alpha_2$  are two different thermal diffusivities corresponding to two simultaneous heat conduction in CNT bundles. The dual- $\alpha$  model assumes two simultaneous thermal transport processes in CNT bundles and considers them independent of each other. As shown in Fig. 3a, the model fits the DTR  $T^*$ -t curves with excellent accuracy.

To study if the DTR phenomenon induced by low temperature is reversible or not, the same sample is measured for three rounds. For the three rounds of cryogenic experiments, the sample is kept inside the vacuum chamber all the time to avoid the influence of environment change. In each round of the cryogenic experiment, the temperature of the cold head is lowered down from 295 K to 10 K and then slowly returned to 295 K. The normalized  $T^*$ -t data for the second and third round at selected temperatures are shown in Fig. 3b and c, respectively. It is found that the temperature of DTR emergence is different for the three rounds. For the first round, the DTR phenomenon emerges at 35 K. For the second round, the DTR phenomenon starts at 55 K and exists at lower temperatures. For the third round, the DTR phenomenon is observed in the whole temperature range of 295–10 K. The physics for the development of the parallel heat transport path under low temperatures will be investigated in the following sections.

## 4. DTR heat conduction by structure separation

## 4.1. Dual-mode thermal diffusivity and structure separation

As shown in Fig. 3, the dual- $\alpha$  model fits the *V-t* curves for the DTR phenomenon in the three round of cryogenic experiment excellently. From this parallel dual- $\alpha$  heat conduction model, two different thermal diffusivity values are determined and denoted correspondingly in Fig. 3. The higher thermal diffusivity is denoted as  $\alpha_1$ , and the lower one is denoted as  $\alpha_2$ . The  $\alpha_1$  and  $\alpha_2$  results are summarized in Fig. 4a. For the first round,  $\alpha_2$  first emerges at 35 K; while for the second round,  $\alpha_2$  appears at 55 K and continues to exist when the temperature is reduced to 10 K. For the third round,  $\alpha_1$  and  $\alpha_2$  are both observed in the whole temperature range of 295–10 K. At 295 K,  $\alpha_1$  (3.72–4.19 × 10<sup>-5</sup> m<sup>2</sup> s<sup>-1</sup>) is 3–4 times higher than that of  $\alpha_2$  (9.91 × 10<sup>-6</sup> m<sup>2</sup> s<sup>-1</sup>). This indicates that for the observed two thermal transport processes illustrated in Fig. 2f, one transfers heat much faster than the other one.

For the one-dimensional heat transfer model expressed in Eq. (4), if an effective sample length  $(L_e)$  instead of the real heat conduction length  $(L_r)$  is used in data fitting, the determined effective  $\alpha$  is proportional to

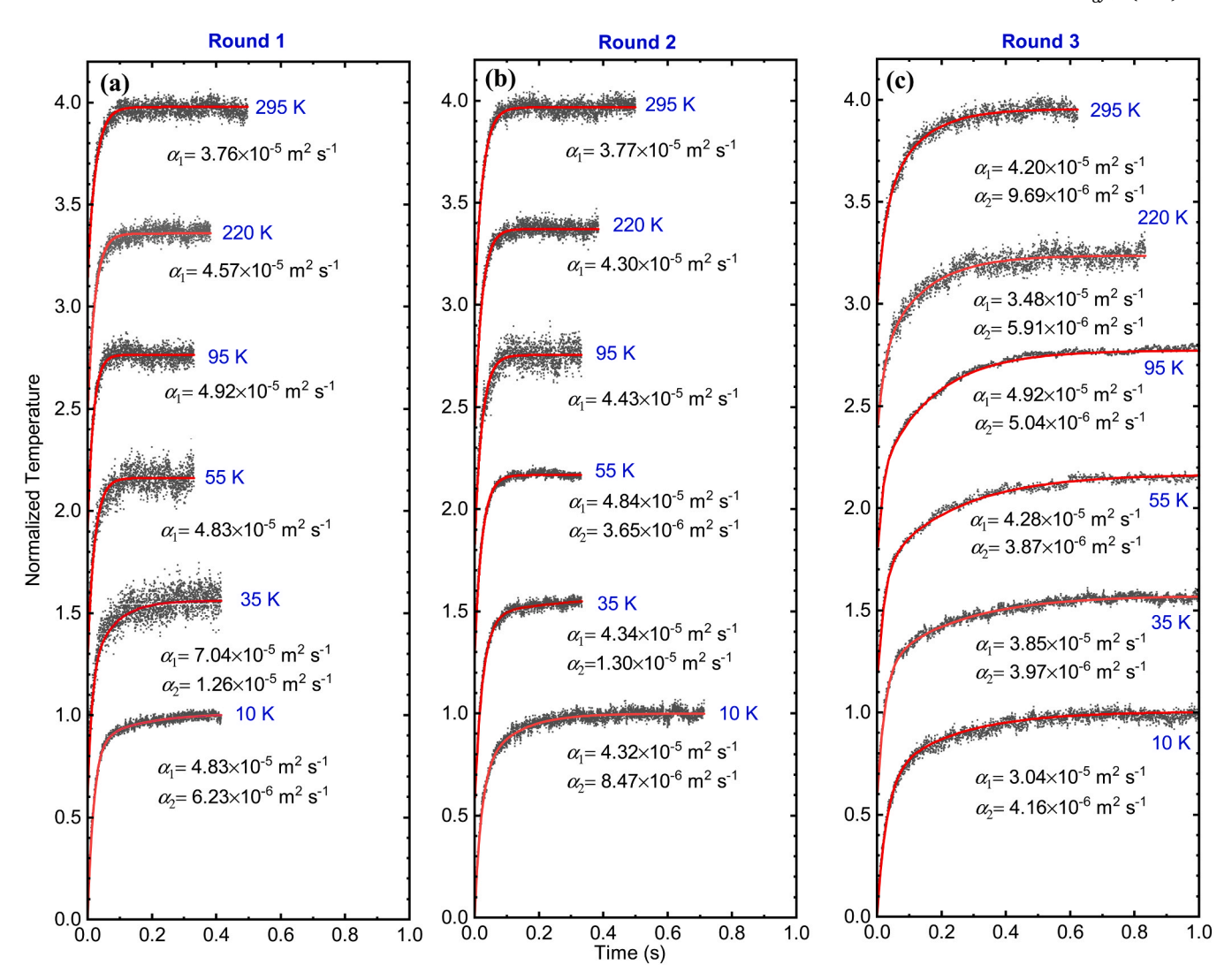


Fig. 3. The normalized temperature rise against time curve with offset during TET characterization for the first round (a), the second round (b), and the third round (c) of cryogenic experiment.

 $L_e^2/L_r^2$ . The coil-shaped CNTs have a much longer real heat transfer path than the straight CNTs. Therefore, if we evaluate the heat transfer at the sample length scale (effective length), the effective  $\alpha$  of straight CNTs will be much higher than that of coiled CNTs. After evaluating several heat transfer paths under SEM, the average ratios of the actual heat transfer route of the coiled CNTs over the axial-direction distance in the sample is estimated to be 1.24. Taking the radial symmetry property of the coiled CNTs into consideration, since  $\sqrt{L_x^2 + L_y^2} = 1.24$ , the 3D ratio of the curvatural length of the coiled CNTs over the straight line length can be determined as  $\sqrt{L_x^2 + L_y^2 + L_z^2} = 1.52$ . Thus, the relationship between the effective thermal diffusivity of the straight CNTs and the coiled CNTs can be calculated as  $\alpha_1 = 1.52^2 \times \alpha_2 = 2.31\alpha_2$ .

Yue et al. reported the thermal property of CNT fibers measured under different elongation ratios and temperatures. They observed a k enhancement of 28% at all temperatures with applied mechanical stretching less than 5% in the axial direction. The value of electrical conductivity showed about 4.4% increase with the elongation [62]. In the randomly oriented sample, the real heat conduction length should be much longer than that in the aligned sample. Thus, if an aligned sample is measured, the thermal diffusivity will be higher than that of the randomly oriented one. In addition, the faster growth speed and higher density of catalyst particles bring in higher density of defects and/or

impurities in the coiled CNTs inevitably, which could also contribute to a lower intrinsic  $\alpha$  of coiled CNTs. This will make the estimated  $\alpha_1/\alpha_2$  ratio even higher than 2.31, closer to the ratio of 3–4 observed in experiments.

As temperature goes down,  $\alpha_1$  shows a slowly increasing pattern from 3.72– $4.19 \times 10^{-5}$  m<sup>2</sup> s<sup>-1</sup> to 2.94– $8.55 \times 10^{-5}$  m<sup>2</sup> s<sup>-1</sup>, while  $\alpha_2$ slowly decreases from  $9.91 \times 10^{-6} \,\mathrm{m}^2 \,\mathrm{s}^{-1}$  to about  $3.70 \times 10^{-6} \,\mathrm{m}^2 \,\mathrm{s}^{-1}$ . For an individual CNT,  $\alpha$  should increase with the decreased temperature according to the thermal reffusivity theory. [45,46] Phonons are the main heat carriers in CNT-based materials. During phonon propagation, phonons encounter scattering from not only other phonons (Umklapp scattering), but also structural defects. To participate in the Umklapp process, the energy of phonons needs to be in the order of  $k_B\theta/2$ , in which  $k_B$  is Boltzmann constant, and  $\theta$  is the Debye temperature [63]. At high temperatures where most phonons are excited, the Umklapp scattering dominates the phonon scattering process. As temperature goes down, the lattice elastic vibration weakens and phonon population decreases. The Umklapp scattering intensity is reduced correspondently, which results in the increased thermal diffusivity [44–46]. While  $\alpha_1$ shows a slowly increasing pattern which agrees well with that of the thermal reffusivity theory,  $\alpha_2$  slowly decreases as temperature goes down from room temperature (RT) to 10 K. This completely reversed trend of  $\alpha_2$  –T indicates a dominating effect of phonon scattering at interfaces among neighboring CNTs [64]. The CNT-CNT contact in  $\alpha_2$  is

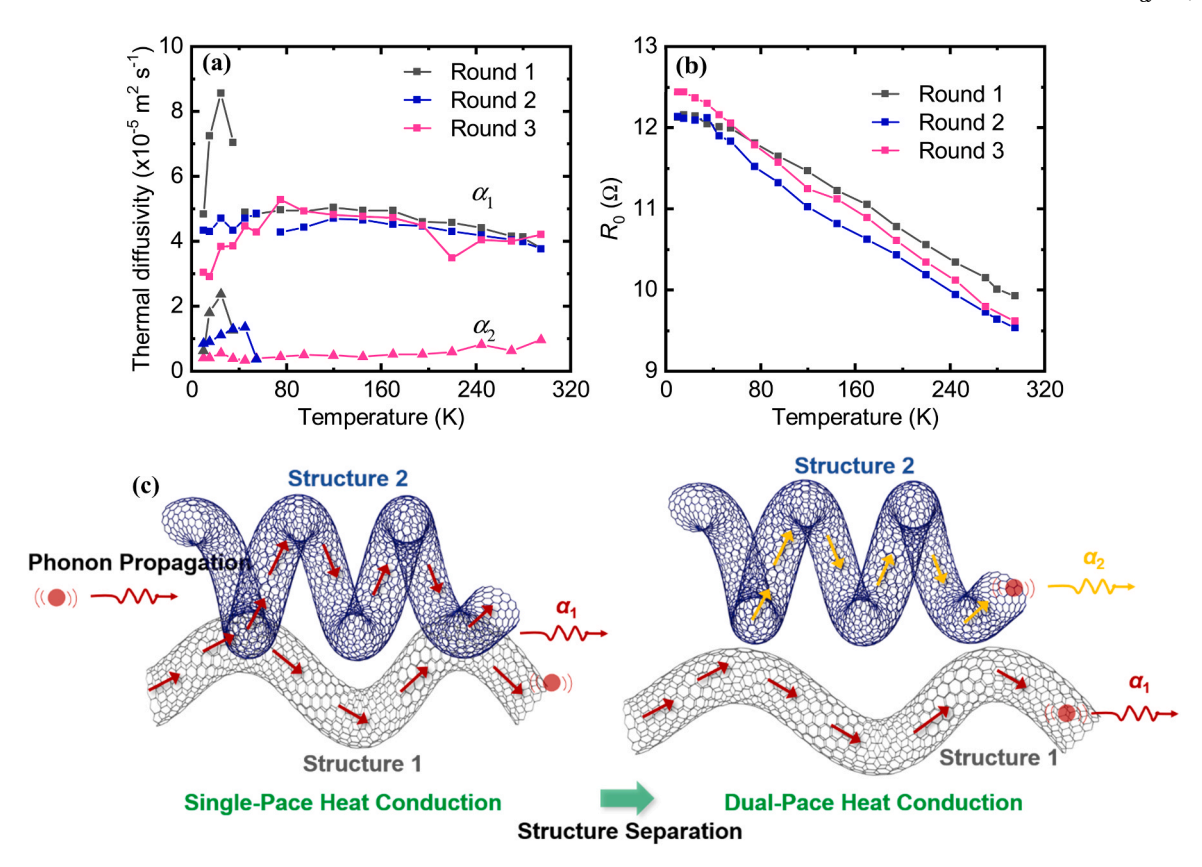


Fig. 4. (a) The measured thermal diffusivity. (b) The electrical resistance of the CNTs bundles. (c) The schematic showing the structure separation process of the two CNTs of different morphologies as temperature goes down.

worsened greatly by the reduced temperature, which even offsets the significantly increasing intrinsic  $\alpha$  pattern with the reduced temperature. Thus, the  $\alpha$ -T curve demonstrates that the dominating mechanism for  $\alpha_1$ -T variation is the Umklapp scattering, while for  $\alpha_2$  is the interfaces phonon scattering. This indicates that in the coiled CNTs, the interface phonon scattering effect is more significant than that in the straight ones.

Fig. 4b shows the measured electrical resistance of the sample for the three rounds of experiments. The  $R_0$ -T curves for the three rounds of experiments present a very similar linearly increasing pattern as temperature goes down. However, the increasing rate dR/dT becomes a little higher from the first round to the third round of cryogenic experiment. A linear fitting can be used to fit the  $R_0$ -T curves for the three rounds of experiments. The fitting result is  $R_0 = 12.35$ –0.0081T for the first round,  $R_0 = 12.28$ –0.0096T for the second round, and  $R_0 = 12.58$ –0.010T for the third round of experiment. The slope of the  $R_0$ -T curves  $(dR_0/dT)$  increases as the cryogenic experiment cycles increase, which indicates  $R_0$  becomes more sensitive to temperature change as the cryogenic experiment cycles increase. Also these R-T relations show that there is no abrupt dR/dT change when T changes. This helps exclude any dR/dT factors in the observed DTR phenomenon.

We speculate that there is a nano-scale structure separation between the relatively straight CNTs and the coiled CNTs in the CNT arrays as temperature goes down, which is responsible for the DTR phenomenon. As shown in Fig. 4c, the two CNTs of coiled and relatively straight morphology are in good contact by Van der Waals (vdW) force at RT before the cryogenic experiment. As temperature goes down, the negative thermal expansion coefficient of CNTs results in the thermal expansion in the length direction. Due to the coiled morphology, the expansion of the coiled CNTs is expected to be much smaller than that of the straight ones in the axial direction. Thus, as the thermal strain is built up by the decreased temperature, a thermal expansion mismatch occurs between the two different CNTs, leading to a structure separation at low

temperatures (35 K for the first round of cryogenic experiment).

In our previous work, we have observed the thermal strain and nanostructure separation generated by temperature variation. By using Raman-based dual thermal probing, the interface spacing change of graphene/Si and graphene/SiO2 interfaces due to the structure separation was evaluated quantitatively on the basis of corrugation-induced Raman enhancement [65]. In addition, when we studied CVD graphene supported on PMMA, we found that part or most of the graphene separated from PMMA when the temperature was reduced to around 150 K [56]. The thermal strain and the structure separation caused by the thermal expansion coefficient (TEC) mismatch between graphene and the substrates, affecting the physical properties of graphene at cryogenic or elevated temperatures, have also been reported in other literatures [66,67]. It is true that there are CNTs with defects in the bundles. However, it is not likely for the bundle with high-quality and low-quality of CNTs to show the same phenomenon. The reason is that in the bundles, the low quality CNTs are in contact with the high quality CNTs. When a joule heating is applied, they are in thermal equilibrium. As a result, the thermal response will show an average effect where only single-pace thermal response can be observed.

For the first round of cryogenic experiment, the structure separation is found to be reversible as temperature is increased up. This is why the V-t curves of the second round of experiment are consistent with that of the first round in the temperature range of 295–75 K. However, the DTR phenomenon begins to appear at 55 K in the second round of cryogenic experiment. This indicates the structure separation becomes easier after the first round of cryogenic experiment. In the third round of cryogenic experiment, the DTR phenomena are observed for the whole temperature range from 295 K to 10 K. This illustrates that the structure separation becomes irreversible after the second round of cryogenic experiment. Such structure separation could also happen among CNTs in contact in the axial direction, leading to reduction of the overall thermal conductivity [confirmed in Fig. 5c]. As reported in the literature, dR/dT

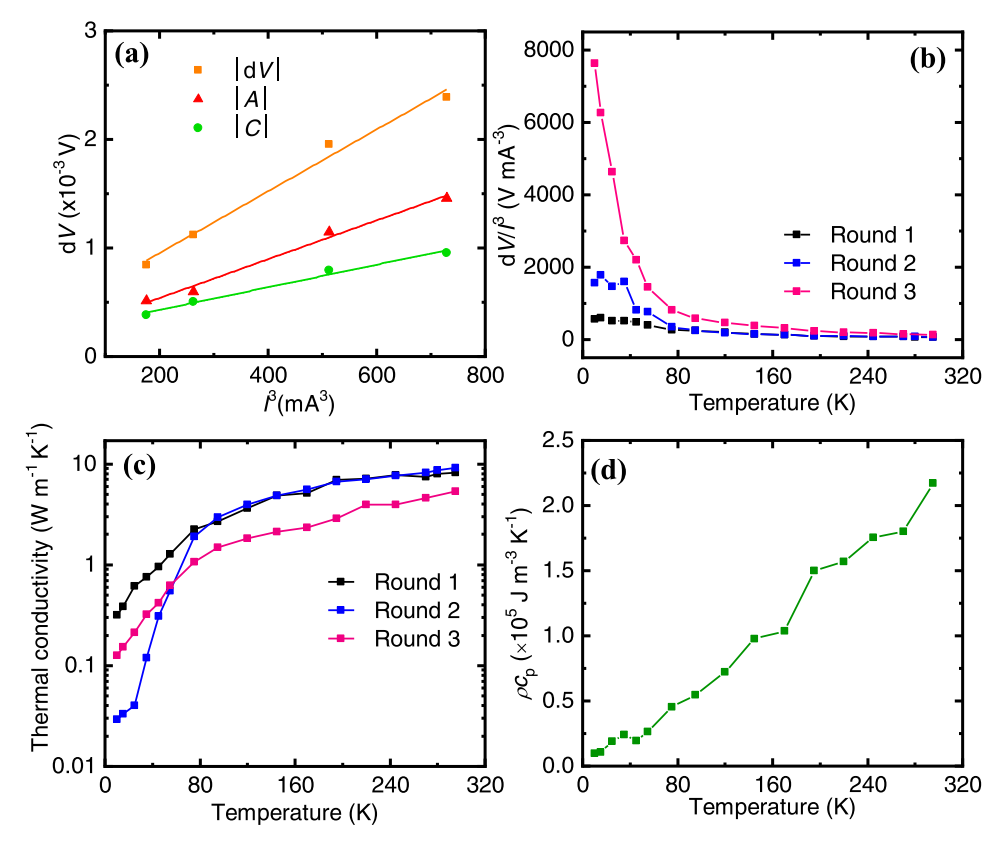


Fig. 5. (a) |dV|, |A|, and |C| against  $I^3$  at 10 K in the third round of experiment. (b)  $dV/I^3$  against temperature illustrating the reduced CNT-CNT contact. (c) The measured apparent thermal conductivity. (d) The volumetric specific heat of the CNTs bundles from the first round of experiment.

of annealed CNTs fibers and isotropic films, as well as acid-doped and iodine-doped fibers showed an evident change at low temperatures [68]. However, the R-T relations for our CNT bundles show that there is no abrupt dR/dT change when T changes. The structure separation leaves very little effect on the electrical resistance, probably due to the electron tunneling effect at the CNT-CNT contact points. Quantitative information about the thermal strain and nano-structure separation generated by temperature increase requires more future investigations. Due to the complexity of the CNT bundle structure, the experiment is extremely challenging and will need very delicate design.

## 4.2. Reduced CNT-CNT contact

The dual-pace thermal response starts to emerge when the temperature of the cold finger is reduced to a certain level. We can control the temperature rise of the sample by adjusting the amplitude of the applied step current. In the TET experiments, we use step currents as small as possible in order to induce a very small joule heating. The temperature rise during the TET characterization is very small, only a few degrees ( $\Delta T$ ≪T). However, when larger step currents are applied, the dual-pace thermal response can still be observed. To confirm the collected V-t signals of DTR in TET characterization are from the joule heating effect, we study the  $dV-I^3$  curves at 10 K as an example. For one-dimensional heat transfer along the CNT bundle, the temperature rise in steady state can be derived as  $\Delta T = I^2 R L / 12 k A_c$ , where  $I^2 R$  is the joule heating power induced by the step current at steady state, L the suspended length of the sample, and  $A_c$  the sample's cross-sectional area [64,69, 70]. It can be seen clearly from this equation that the temperature rise of the sample induced by the joule heating effect is proportional to the supplied current as:  $\Delta T \propto I^2$ . In a small temperature range, the change of electrical resistance  $\Delta R$  can be considered proportional to  $\Delta T$ . Therefore, if the voltage change in the TET signals is induced by the small joule heating effect, the resulting voltage change  $[dV = V(t \rightarrow \infty) - V_0]$  should be linearly related to  $I^3$  as  $dV \propto I^3$ .

As shown in Fig. 5a, the absolute value of dV at 10 K in the third round of experiment shows a good linear relationship with  $I^3$ , which clearly confirms the joule heating effect. Furthermore, for the dual- $\alpha$  physics model in Eq. (5), the coefficient A and C are proportional to the voltage change induced by the two different thermal diffusivities  $\alpha_1$  and  $\alpha_2$  respectively. The corresponding absolute values of A and C resulted from the four different step currents are also presented in Fig. 5a. It can be seen clearly that both |A| and |C| also show a good linear relationship with  $I^3$ . These results firmly demonstrate that the observed DTR signals in the TET experiment are resulted from joule heating. There must be two heat transfer channels responsible for the observed dual-paced thermal response.

To understand the corresponding micro-structure evolution governing this DTR process, the  $dV/I^3$  against temperature curves are calculated. As presented in Fig. 5b,  $dV/I^3$  increases as temperature goes down. For the first round of cryogenic experiment,  $dV/I^3$  slowly increases from  $70.36 \text{ V mA}^{-3}$  at 295 K to 569.51 V mA<sup>-3</sup> at 10 K, which is 8-fold increase. For the second round of cryogenic experiment,  $dV/I^3$  shows a faster increase from 70.36 V  $mA^{-3}$  at 295 K to 1572.19 V  $mA^{-3}$  at 10 K, which is 22-fold increase. For the third round of experiment,  $dV/I^3$  increases sharply from 116.67 V mA $^{-3}$  at 295 K to 7630.54 V mA $^{-3}$  at 10 K, which is 65-fold increase. The overall voltage change is  $dV = I \cdot \Delta R = I \cdot \Delta T \cdot dR/dT$ . At steady state, we have  $\Delta T = I^2 R L/(12A_c \cdot k)$ . Therefore,  $dV/I^3 = RLdR/dT/(12A_c \cdot k)$ , where  $A_c$  is the cross-sectional area of the sample. As shown in Fig. 4b, R and dR/dT change little from round 1 to round 3. Therefore the changes of  $dV/I^3$  from round 1 to round 3 mostly are induced by the change of thermal conductivity k. The joule heating during TET characterization can reverse some of the structure separation while the number of contacts that can be recovered is limited. This explains the significantly increased  $dV/I^3$  uncovered in

the experiments.

The apparent thermal conductivity  $(k_m)$  is characterized by using the steady-state electro-thermal (SET) technique [64,69,70]. The experimental set-up is same as that of the TET technique. In this method, k at each temperature is obtained by:  $k_m = I^2RL(dR/dT)/12A_c\Delta R$ . In the equation,  $k_m$  is the apparent thermal conductivity, I the DC current flowing through the sample, R the resistance of the sample at steady state, dR/dT is obtained by differentiating the  $R_0$ -T curve, and  $\Delta R$  the resistance change induced by the joule heating. The resulting thermal radiation effect is calculated and found to take less than 2% of  $k_m$ . Therefore, the error from the thermal radiation effect is insignificant on the final result. The measurement uncertainty of SET is estimated to be about  $\pm 10\%$ . For clarity of comparison, the error bars are omitted in the figure.

Fig. 5c shows the result of  $k_m$  for the three rounds of cryogenic experiments. In the first round,  $k_m$  undergoes a decreasing pattern from  $9.14~\mathrm{W~m^{-1}~K^{-1}}$  to  $0.32~\mathrm{W~m^{-1}~K^{-1}}$  as temperature goes down from 295 K to 10 K, which shows a quartic relation with temperature. In the second round of cryogenic experiment, the measured  $k_m$  presents a good consistency with that of the first round in the temperature range of 295–75 K. However, as temperature is further lowered down to 55 K, k begins to drop fast and significantly deviates from  $k_m$  of the first round, which decreases from 1.90 W m $^{-1}$  K $^{-1}$  at 75 K to 0.03 W m $^{-1}$  K $^{-1}$  at 10 K. For the third round of experiment, k decreases from 5.32 W m<sup>-1</sup> K<sup>-1</sup> to 0.13 W m<sup>-1</sup> K<sup>-1</sup>, following a quartic relation with temperature, which is a very similar decreasing pattern as that of the first round. Nevertheless, the value of  $k_m$  is 1.72–2.55 times lower than that of the first round in the whole temperature range of 295-10 K. This indicates the micro-structure of the CNT array undergoes an irreversible change after the second round of cryogenic experiment.

The volumetric specific heat  $(\rho c_p)$  against temperature profile is obtained using the measured thermal diffusivity  $\alpha_1$  and measured thermal conductivity  $k_m$  in the first round of experiment as  $\rho c_p = k_m/\alpha_m$ . Fig. 5d shows the resulting volumetric specific heat.  $\rho c_p$  decreases linearly with the trend similar to that of graphite. As temperature goes to zero, the specific heat goes to zero. Since  $\alpha_1$  is dominated by the intrinsic thermal properties of the CNTs as illustrated in the thermal diffusivity discussion above, this result demonstrates the good accuracy of the  $k_m$  and  $\alpha_m$  result. Based on the measured volumetric specific heat of the bundle and the specific heat of graphite at 295 K ( $c_p = 710$  J kg $^{-1}$  K $^{-1}$ ), [71] the density of the bundle is estimated to be 316.9 kg m $^{-3}$ . The porosity can be obtained as  $\varphi = (1-\rho_{\text{bundle}}/\rho_{\text{graphite}}) \times 100\%$ , where  $\rho_{\text{bundle}}$  and  $\rho_{\text{graphite}}$  are the density of the bundle and graphite (2230 kg m $^{-3}$ ). The porosity is determined to be 85.8%.

## 4.3. The parallel heat transfer model

In this section, the proportion of the straight CNTs and coiled CNTs under different temperatures will be investigated to have a closer look at the structure evolution. For the two parallel resistances  $R_1$  and  $R_2$  as shown in Fig. 2f, we have:

$$\Delta R = \frac{\Delta R_1 R_2^2}{(R_1 + R_2)^2} + \frac{\Delta R_2 R_1^2}{(R_1 + R_2)^2}.$$
 (6)

If the temperature coefficient of resistance for the two parallel resistances is assume to be  $\beta_1$  and  $\beta_2$ , respectively, the overall temperature coefficient of resistance (dR/dT) can be derived as:

$$\frac{dR}{dT} = \frac{\beta_1 R_2^2}{(R_1 + R_2)^2} + \frac{\beta_2 R_1^2}{(R_1 + R_2)^2}.$$
 (7)

Thus, the overall temperature change ( $\Delta T$ ) due to joule heating, which is obtained as  $\Delta T = \Delta R / (dR/dT)$ , can be derived by combining Eqs. (6) and (7) as:

$$\Delta T = \frac{\Delta R_1 R_2^2 + \Delta R_2 R_1^2}{\beta_1 R_2^2 + \beta_2 R_1^2}.$$
 (8)

Since for the two resistance,  $\Delta R_1 = \Delta T_1 \cdot \beta_1$  and  $\Delta R_2 = \Delta T_2 \cdot \beta_2$ , we have:

$$\Delta T = \frac{\beta_1 R_2^2 \Delta T_1 + \beta_2 R_1^2 \Delta T_2}{\beta_1 R_2^2 + \beta_2 R_2^2}.$$
 (9)

For each heat transfer path, its temperature rise is  $\Delta T = V^2 L/(12RA_ck)$ . Here L and  $A_c$  are the real heat transfer length and cross-sectional area, respectively. If we assume the two structures have the same intrinsic thermal conductivity and electrical resistivity, and their only difference is the morphology, then we have  $\Delta T_1 = \Delta T_2$ . Such assumption is physically reasonable since the two structures follow the same growth mechanisms. This conclusion also tells that during the dual-path heat conduction, there is no heat exchange between the two structures. Then it can be seen clearly that the overall temperature rise is equal to that of the two parallel resistances,  $\Delta T = \Delta T_1 = \Delta T_2$ .

During the TET characterization, dV is related to I as  $dV = I \cdot \Delta R$ . Combined with Eq. (6), we have:

$$\Delta V = \frac{I_0 \Delta R_1 R_2^2}{\left(R_1 + R_2\right)^2} + \frac{I_0 \Delta R_2 R_1^2}{\left(R_1 + R_2\right)^2}.$$
 (10)

Since  $\Delta R_1 = \Delta T \cdot \beta_1$  and  $\Delta R_2 = \Delta T \cdot \beta_2$ , and it has been demonstrated above that the overall temperature rise is equal to that of the two parallel resistances,  $\Delta T = \Delta T_1 = \Delta T_2$ , the voltage change can be derived as:

$$\Delta V = I_0 \Delta T \frac{\beta_1 R_2^2}{(R_1 + R_2)^2} + I_0 \Delta T \frac{\beta_2 R_1^2}{(R_1 + R_2)^2}.$$
 (11)

Combining the dual- $\alpha$  thermal transport model in Eq. (5), for the two different morphologies of CNTs, we have  $A \propto I_0 \Delta T \beta_1 R_2^2/(R_1+R_2)^2$  and  $C \propto I_0 \Delta T \beta_2 R_1^2/(R_1+R_2)^2$ . Therefore, the ratio A/C can be expressed as  $A/C=(\beta_1/\beta_2)\cdot(R_2^2/R_1^2)$ . As shown in Fig. 6a, A/C is less than 1 in the temperature range of 55–295 K, while it increases to more than 2 at temperatures below 15 K. This result indicates that although  $R_2$  is larger than  $R_1$ , the increasing rate of  $R_2$  is faster than that of  $R_1$ , which makes  $R_2$  much higher than  $R_1$  at relatively high temperatures. This is because structure 2 has fewer CNT-CNT contacts than structure 1. The much higher  $R_2$  results in the ratio of  $R_2$  less than 1. While at very low temperatures (below 55 K), since the value of  $R_2$  increases to very high value, the term  $(R_2^2/R_1^2)$  becomes dominating in  $R_2$ , which makes  $R_2$  increases to a value higher than 2.

If we assume that the total cross-sectional area of the CNTs bundle is  $A_c$ , the proportion that structure 1 (relatively straight CNTs) takes is  $A_1^*$ , and the proportion that structure 2 (coiled CNTs) takes is  $A_2^*$ , then the real cross-sectional area of structure 1 and structure 2 is  $A_1 = A_c \cdot A_1^*$  and  $A_2 = A_c \cdot A_2^*$ , respectively. Note  $A_c$  for the total CNT bundle includes the effect of open space among CNTs.  $A_1$  and  $A_2$  for the relatively straight and coiled CNTs are only for the area of the solid part. Also we assume the real heat transfer path of structure 1 and structure 2 is  $L_1$  and  $L_2$ , respectively. For the one-dimensional heat transfer model in steady state, the apparent thermal conductivity can be derived as  $k_{\rm eff} = (V^2/R) \cdot L/(12\Delta TA_c)$ , where  $V^2/R$  is the joule heating power induced by the step current, L is the suspended length of the sample [64,69]. Combined with the parallel resistance model, by simple mathematical derivation,  $k_{\rm eff}$  can be expressed as:

$$k_{eff} = \frac{V^2 L_1}{12A_1 \Delta T \cdot R_1} \cdot \frac{A_1}{A_c} \cdot \frac{L}{L_1} + \frac{V^2 L_2}{12A_2 \Delta T R_2} \cdot \frac{A_2}{A_c} \cdot \frac{L}{L_2}.$$
 (12)

In addition, from Eq. (4), it can be seen clearly that the effective thermal diffusivity is reversely proportional to the square of real heat transfer length, which leads to  $\sqrt{\alpha_1} \propto L/L_1$  and  $L/L_2 \propto \sqrt{\alpha_2}$ . For the one-dimensional heat transfer model in steady state, the intrinsic thermal conductivity of structure 1 and structure 2 can also be expressed as  $k_1 = 1$ 

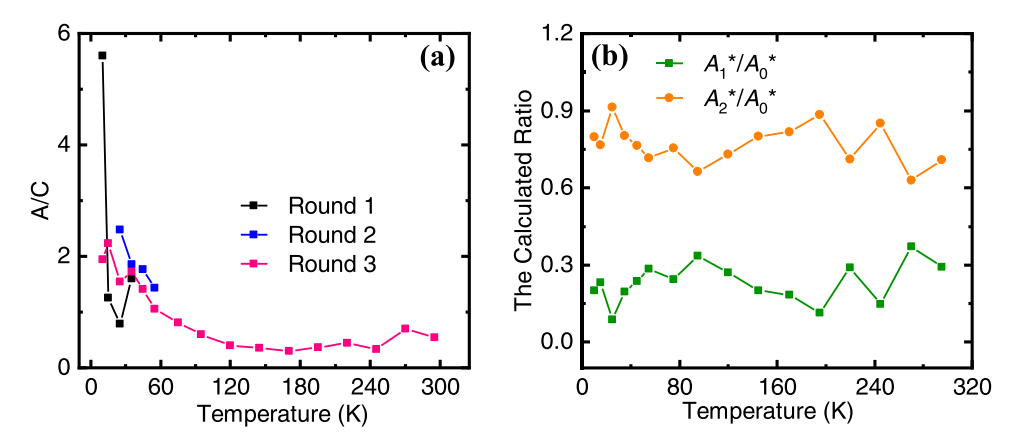


Fig. 6. (a) The ratio of A/C and (b) the ratio of the calculated normalized area of the two different CNTs for the further analysis of the nano-scale structure separation.

 $(V^2/R_1)L_1/(12A_1\Delta T)$  and  $k_2=(V^2/R_2)L_2/(12A_2\Delta T)$ . The intrinsic thermal conductivity  $k_1$  and  $k_2$  can be regarded as equal to a constant k. Therefore, after the structure separation,  $k_{\rm eff}$  can be expressed as

$$k_{eff,2} = nA_1^* \sqrt{\alpha_1} + nA_2^* \sqrt{\alpha_2},\tag{13}$$

where  $n \propto k$  is a constant. While before the structure separation, we have

$$k_{eff,1} = nA_0^* \sqrt{\alpha_1},\tag{14}$$

where  $A_0^* = A_1^* + A_2^*$  is the total cross-sectional area of structure 1 and structure 2. By combining Eqs. (13) and (14), using the experimental data of apparent thermal conductivity from the first round of cryogenic experiment as  $k_{\text{eff},1}$  (before structure separation) and that from the third round of cryogenic experiment as  $k_{\rm eff,2}$  (after structure separation), the ratio of the normalized cross-sectional area of structure 1 and structure 2 can be calculated. Fig. 6b presents the results of  $A_1^*/A_0^*$  and  $A_2^*/A_0^*$ . It can be seen that  $A_1^*/A_0^*$  stays almost constant at around 0.2, while  $A_2^*/A_0^*$  at around 0.8. This indicates that after the structure separation, the proportion of structure 1 in the cross section is about 20% while that of structure 2 is about 80%. Therefore, the coiled CNTs play a dominating role in the thermal conduction process of the CNTs bundles after the structure separation. As shown in Fig. 4c, before structure separation (round 1 and round 2), structure 1 (relatively straight CNTs) are in good contact with the coiled ones. This provides some shortcuts of heat conduction in structure 2 (coiled CNTs). Thus, heat does not have to flow over a long distance in the coiled CNTs. Nevertheless, after the structure separation, heat has to flow in the coiled CNTs, making the effective thermal diffusivity and conductivity lower.

The dual-pace thermal response can be a common feature for VACNTs with two morphologies under certain conditions. For the dual-pace thermal response to occur, there needs to be both straight and coiled morphologies in the VACNTs. In addition, they need to be separated from each other so as to transfer heat independently. Under this circumstance, it is expected to also show the similar dual-pace thermal response. How strong the dual-pace signals can be depends on the ratio of the two morphologies. If the proportion of the separated straight and coiled nanotubes are comparable, it is very likely to show a strong dual-pace transient heat transfer; while if one morphology significantly dominates in the structure, it is possible that only a single-pace thermal response will be observed since the other one could be overshadowed.

### 5. Conclusions

In this work, an abnormal DTR phenomenon in vertically aligned CNT arrays was discovered under TET characterization. Three rounds of cryogenic experiments were conducted to confirm and investigate the emergence of the DTR phenomenon. As temperature decreased, the DTR

phenomenon emerged at a certain temperature and existed over the lower temperatures. Such phenomenon became permanent over all the temperatures of 295-10 K after two rounds of cryogenic experiments. The voltage change in TET signals was found to be linearly related to  $I^3$ , confirming the DTR phenomenon was induced by joule heating. The DTR voltage-time profiles can be fitted using two thermal diffusivities, reflecting a dual-pace transient thermal response. As temperature went down, the larger thermal diffusivity  $(\alpha_1)$  showed a slowly increasing pattern from  $3.72-4.19 \times 10^{-5} \text{ m}^2 \text{ s}^{-1}$  to  $2.94-8.55 \times 10^{-5} \text{ m}^2 \text{ s}^{-1}$ while the smaller thermal diffusivity ( $\alpha_2$ ) slowly decreased from  $9.91 \times 10^{-6} \, \text{m}^2 \, \text{s}^{-1}$  to about  $3.70 \times 10^{-6} \, \text{m}^2 \, \text{s}^{-1}$ . The unique structure of CNT bundles constitutes parallel heat conduction paths which result in DTR. The nano-scale structure separation induced by the increased thermal strain led to a thermal diffusivity/conductivity separation phenomenon. To understand the corresponding micro-structure evolution governing this DTR process, the  $dV/I^3$  against temperature curves were calculated. The significantly increased  $dV/I^3$  in the experiments uncovered the reduced CNT-CNT contact as temperature went down. The measured thermal conductivity variation against temperature also supported the proposed structure separation model. By further building a new parallel heat transfer model taking both the transient and steadystate electrical and thermal response into consideration, the ratio of the cross-sectional area of the separated two different CNTs was determined. It was found that the coiled CNTs played a dominant role in the thermal conduction process after structure separation. Our findings uncovered that coiled CNTs and nano-structure evolution of CNTs could have significant effect on the thermal and electrical transport of CVD grown CNTs arrays, especially their transient responses. The dual-pace thermal response can be a common feature for VACNTs with two separated morphologies. The developed parallel heat transfer model will be of great value in analyzing experimental results and designing CNTs arrays for various applications.

## CRediT authorship contribution statement

The manuscript was written through contributions of all authors. All authors have given approval to the final version of the manuscript.

## **Declaration of Competing Interest**

The authors declare that they have no known competing financial interests or personal relationships that could have appeared to influence the work reported in this paper.

## Acknowledgments

Support of this work by National Natural Science Foundation of

China, China (No. 51906161), Natural Science Foundation of Guangdong Province, China (No. 2020A1515011186), the Start-up Fund of Shenzhen University and Scientific Research Foundation for Talented Scholars in Shenzhen, China is gratefully acknowledged. X.W is grateful for the support by US National Science Foundation, USA (CBET1930866 and CMMI2032464). The work by G.E. was supported by the U.S. Department of Energy (DOE), Office of Science, Basic Energy Sciences (BES), Materials Sciences and Engineering Division, USA.

### Funding

This work was supported by the National Natural Science Foundation of China [No. 51906161], Natural Science Foundation of Guangdong Province [No. 2020A1515011186], US National Science Foundation [CBET1930866 and CMMI2032464], U.S. Department of Energy (DOE), Office of Science, Basic Energy Sciences (BES), Materials Sciences and Engineering Division.

#### References

- E. Pop, D. Mann, Q. Wang, K.E. Goodson, H.J. Dai, Thermal conductance of an individual single-wall carbon nanotube above room temperature, Nano Lett. 6 (1) (2006) 96–100, https://doi.org/10.1021/nl052145f.
- [2] C. Silvestri, M. Riccio, R.H. Poelma, A. Jovic, B. Morana, S. Vollebregt, A. Irace, G. Zhang, P.M. Sarro, Effects of conformal nanoscale coatings on thermal performance of vertically aligned carbon nanotubes, Small 14 (20) (2018), e1800614, https://doi.org/10.1002/smll.201800614.
- [3] Y. Cohen, S.K. Reddy, Y. Ben-Shimon, A. Ya'akobovitz, Height and morphology dependent heat dissipation of vertically aligned carbon nanotubes, Nanotechnology 30 (50) (2019), 505705, https://doi.org/10.1088/1361-6528/ ab424e.
- [4] B.R. Lettiere, C.A.C. Chazot, K.H. Cui, A.J. Hart, High-density carbon nanotube forest growth on copper foil for enhanced thermal and electrochemical interfaces, ACS Appl. Nano Mater. 3 (1) (2020) 77–83, https://doi.org/10.1021/ acsanm.9b01595.
- [5] Y. Yang, L. Liu, Y. Wei, P. Liu, K. Jiang, Q. Li, S. Fan, In situ fabrication of HFC-decorated carbon nanotube yarns and their field-emission properties, Carbon 48 (2) (2010) 531–537, https://doi.org/10.1016/j.carbon.2009.09.074.
- [6] W. Li, J. Yuan, A. Dichiara, Y. Lin, J. Bai, The use of vertically aligned carbon nanotubes grown on SiC for in situ sensing of elastic and plastic deformation in electrically percolative epoxy composites, Carbon 50 (11) (2012) 4298–4301, https://doi.org/10.1016/j.carbon.2012.05.011.
- [7] P. La Torraca, M. Bobinger, M. Servadio, P. Pavan, M. Becherer, P. Lugli, L. Larcher, On the frequency response of nanostructured thermoacoustic loudspeakers, Nanomaterials 8 (10) (2018) 833, https://doi.org/10.3390/ page-10.0929
- [8] L. Xiao, Z. Chen, C. Feng, L. Liu, Z.Q. Bai, Y. Wang, L. Qian, Y.Y. Zhang, Q.Q. Li, K. L. Jiang, S.S. Fan, Flexible, stretchable, transparent carbon nanotube thin film loudspeakers, Nano Lett. 8 (12) (2008) 4539–4545, https://doi.org/10.1021/nl802750z.
- [9] P. Liu, L. Liu, Y. Wei, K. Liu, Z. Chen, K.L. Jiang, Q.Q. Li, S.S. Fan, Fast high-temperature response of carbon nanotube film and its application as an incandescent display, Adv. Mater. 21 (35) (2009) 3563–3566, https://doi.org/10.1002/adma.200900473
- [10] Z. Yin, H. Wang, M. Jian, Y. Li, K. Xia, M. Zhang, C. Wang, Q. Wang, M. Ma, Q. Zheng, Y. Zhang, Extremely black vertically aligned carbon nanotube arrays for solar steam generation, ACS Appl. Mater. Interfaces 9 (34) (2017) 28596–28603, https://doi.org/10.1021/acsami.7b08619.
- [11] S. Murata, M. Imanishi, S. Hasegawa, R. Namba, Vertically aligned carbon nanotube electrodes for high current density operating proton exchange membrane fuel cells, J. Power Sources 253 (2014) 104–113, https://doi.org/10.1016/j. jpowsour.2013.11.073.
- [12] K. Jiang, Q. Li, S. Fan, Spinning continuous carbon nanotube yarns, Nature 419 (6909) (2002) 801, https://doi.org/10.1038/419801a.
- [13] M. Zhang, K.R. Atkinson, R.H. Baughman, Multifunctional carbon nanotube yarns by downsizing an ancient technology, Science 306 (5700) (2004) 1358–1361, https://doi.org/10.1126/science.1104276.
- [14] C.J. Lee, K.H. Son, J. Park, J.E. Yoo, Y. Huh, J.Y. Lee, Low temperature growth of vertically aligned carbon nanotubes by thermal chemical vapor deposition, Chem. Phys. Lett. 338 (2–3) (2001) 113–117, https://doi.org/10.1016/S0009-2614(00) 01378-6.
- [15] K. Jiang, J. Wang, Q. Li, L. Liu, C. Liu, S. Fan, Superaligned carbon nanotube arrays, films, and yarns: a road to applications, Adv. Mater. 23 (9) (2011) 1154–1161, https://doi.org/10.1002/adma.201003989.
- [16] H. Wang, Z. Xu, G. Eres, Order in vertically aligned carbon nanotube arrays, Appl. Phys. Lett. 88 (21) (2006), 213111, https://doi.org/10.1063/1.2206152.
- [17] D. Wang, Y. Lei, W. Jiao, Y. Liu, C. Mu, X. Jian, A review of helical carbon materials structure, synthesis and applications, Rare Met. 40 (1) (2020) 3–19, https://doi. org/10.1007/s12598-020-01622-y.

- [18] C.J. Lee, J. Park, S. Han, J. Ihm, Growth and field emission of carbon nanotubes on sodalime glass at 550 degrees C using thermal chemical vapor deposition, Chem. Phys. Lett. 337 (4–6) (2001) 398–402, https://doi.org/10.1016/S0009-2614(01) 00232.0
- [19] L. Li, L. Lu, S. Qi, Preparation, characterization and microwave absorption properties of porous nickel ferrite hollow nanospheres/helical carbon nanotubes/ polypyrrole nanowires composites, J. Mater. Sci. Mater. Electron. 29 (10) (2018) 8513–8522, https://doi.org/10.1007/s10854-018-8865-y.
- [20] Y. Gao, F. Guo, P. Cao, J. Liu, D. Li, J. Wu, N. Wang, Y. Su, Y. Zhao, Winding-locked carbon nanotubes/polymer nanofibers helical yarn for ultrastretchable conductor and strain sensor, ACS Nano 14 (3) (2020) 3442–3450, https://doi.org/10.1021/ acspano.9b09533.
- [21] W. Chen, J. Zhang, Y. Yue, Molecular dynamics study on thermal transport at carbon nanotube interface junctions: effects of mechanical force and chemical functionalization, Int. J. Heat Mass Transf. 103 (2016) 1058–1064, https://doi. org/10.1016/j.ijheatmasstransfer.2016.08.016.
- [22] K. Bui, B.P. Grady, D.V. Papavassiliou, Heat transfer in high volume fraction CNT nanocomposites: effects of inter-nanotube thermal resistance, Chem. Phys. Lett. 508 (4–6) (2011) 248–251, https://doi.org/10.1016/j.cplett.2011.04.005.
- [23] C. Nan, G. Liu, Y. Lin, M. Li, Interface effect on thermal conductivity of carbon nanotube composites, Appl. Phys. Lett. 85 (16) (2004) 3549–3551, https://doi. org/10.1063/1.1808874.
- [24] A.K. Vallabhaneni, B. Qiu, J. Hu, Y.P. Chen, A.K. Roy, X.L. Ruan, Interfacial thermal conductance limit and thermal rectification across vertical carbon nanotube/graphene nanoribbon-silicon interfaces, J. Appl. Phys. 113 (6) (2013), 064311, https://doi.org/10.1063/1.4790367.
- [25] C. Deng, C. Li, P. Wang, X. Wang, L. Pan, Revealing the linear relationship between electrical, thermal, mechanical and structural properties of carbon nanocoils, PCCP 20 (19) (2018) 13316–13321, https://doi.org/10.1039/c8cp01349g.
- [26] Y. Xie, T. Wang, B. Zhu, C. Yan, P. Zhang, X. Wang, G. Eres, 19-fold thermal conductivity increase of carbon nanotube bundles toward high-end thermal design applications, Carbon 139 (2018) 445–458, https://doi.org/10.1016/j. carbon.2018.07.009.
- [27] C. Yu, G. Zhang, The underestimated thermal conductivity of graphene in thermal-bridge measurement: a computational study, J. Appl. Phys. 113 (21) (2013), 214304. https://doi.org/10.1063/1.4809554.
- [28] T. Borca-Tasciuc, A.R. Kumar, G. Chen, Data reduction in 3ω method for thin-film thermal conductivity determination, Rev. Sci. Instrum. 72 (4) (2001) 2139–2147, https://doi.org/10.1063/1.1353189.
- [29] M. Sheindlin, D. Halton, M. Musella, C. Ronchi, Advances in the use of laser-flash techniques for thermal diffusivity measurement, Rev. Sci. Instrum. 69 (3) (1998) 1426–1436, https://doi.org/10.1063/1.1148776.
- [30] Y. Yue, X. Huang, X. Wang, Thermal transport in multiwall carbon nanotube buckypapers, Phys. Lett. A 374 (40) (2010) 4144–4151, https://doi.org/10.1016/j. physleta.2010.08.034.
- [31] Y. Hu, A. Fan, H. Wang, W. Ma, X. Zhang, Dual-wavelength flash raman mapping method for measuring thermal diffusivity of the suspended nanowire, Sci. China Technol. Sci. 63 (5) (2020) 748–754, https://doi.org/10.1007/s11431-019-9558-3
- [32] A. Fan, Y. Hu, H. Wang, W. Ma, X. Zhang, Dual-wavelength flash Raman mapping method for measuring thermal diffusivity of suspended 2D nanomaterials, Int. J. Heat Mass Transf. 143 (2019) 118460.1–118460.9, https://doi.org/10.1016/j. iiheatmasstransfer 2019 118460
- [33] R. Wang, S. Xu, Y. Yue, X. Wang, Thermal behavior of materials in laser-assisted extreme manufacturing: Raman-based novel characterization, Int. J. Extrem. Manuf. 2 (2020), 032004, https://doi.org/10.1088/2631-7990/aba17c.
- [34] M. Bauer, Q. Pham, C. Saltonstall, P. Norris, Thermal conductivity of vertically aligned carbon nanotube arrays: growth conditions and tube inhomogeneity, Appl. Phys. Lett. 105 (15) (2014), 151909, https://doi.org/10.1063/1.4898708.
- [35] X. Huang, J. Wang, G. Eres, X. Wang, Thermophysical properties of multi-wall carbon nanotube bundles at elevated temperatures up to 830 K, Carbon 49 (5) (2011) 1680–1691, https://doi.org/10.1016/j.carbon.2010.12.053.
- [36] I. Ivanov, A. Puretzky, G. Eres, H. Wang, Z.W. Pan, H.T. Cui, R.Y. Jin, J. Howe, D. B. Geohegan, Fast and highly anisotropic thermal transport through vertically aligned carbon nanotube arrays, Appl. Phys. Lett. 89 (22) (2006), 223110, https://doi.org/10.1063/1.2397008.
- [37] D. Yang, Q. Zhang, G. Chen, S.F. Yoon, J. Ahn, S. Wang, Q. Zhou, Q. Wang, J. Li, Thermal conductivity of multiwalled carbon nanotubes, Phys. Rev. B 66 (16) (2002), 165440, https://doi.org/10.1103/PhysRevB.66.165440.
- [38] J. Hone, M. Whitney, C. Piskoti, A. Zettl, Thermal conductivity of single-walled carbon nanotubes, Synth. Met. 103 (4) (1999) 2514–2516, https://doi.org/ 10.1016/S0379-6779(98)01070-4.
- [39] J. Wang, M. Gu, X. Zhang, G. Wu, Measurements of thermal effusivity of a fine wire and contact resistance of a junction using a T type probe, Rev. Sci. Instrum. 80 (7) (2009), 076107, https://doi.org/10.1063/1.3159863.
- [40] J. Yang, S. Waltermire, Y. Chen, A.A. Zinn, T.T. Xu, D. Li, Contact thermal resistance between individual multiwall carbon nanotubes, Appl. Phys. Lett. 96 (2) (2010) 023109.1–023109.3, https://doi.org/10.1063/1.3292203.
- [41] Q. Li, K. Katakami, T. Ikuta, M. Kohno, X. Zhang, K. Takahashi, Measurement of thermal contact resistance between individual carbon fibers using a laser-flash raman mapping method, Carbon 141 (2019) 92–98, https://doi.org/10.1016/j. carbon.2018.09.034.
- [42] H. Zhang, J. Li, K. Yao, L. Chen, Spark plasma sintering and thermal conductivity of carbon nanotube bulk materials, J. Appl. Phys. 97 (11) (2005), 114310, https://doi.org/10.1063/1.1927286.

- [43] J. Guo, X. Wang, D.B. Geohegan, G. Eres, C. Vincent, Development of pulsed laser-assisted thermal relaxation technique for thermal characterization of microscale wires, J. Appl. Phys. 103 (11) (2008), 113505, https://doi.org/10.1063/1.2936873
- [44] C. Deng, Y. Sun, L. Pan, T. Wang, Y. Xie, J. Liu, B. Zhu, X. Wang, Thermal diffusivity of a single carbon nanocoil: uncovering the correlation with temperature and domain size, ACS Nano 10 (10) (2016) 9710–9719, https://doi. org/10.1021/acsnano.6b05715.
- [45] Y. Xie, B. Zhu, J. Liu, X.U. Zaoli, X. Wang, Thermal reffusivity: uncovering phonon behavior, structural defects, and domain size, Front. Energy 12 (1) (2018) 143–157, https://doi.org/10.1007/s11708-018-0520-z.
- [46] Y. Xie, Z. Xu, S. Xu, Z. Cheng, N. Hashemi, C. Deng, X. Wang, The defect level and ideal thermal conductivity of graphene uncovered by residual thermal reffusivity at the 0 K limit, Nanoscale 7 (22) (2015) 10101–10110, https://doi.org/10.1039/ c5nr02012c.
- [47] Z. Xu, X. Wang, H. Xie, Promoted electron transport and sustained phonon transport by DNA down to 10 K, Polymer 55 (24) (2014) 6373–6380, https://doi. org/10.1016/j.polymer.2014.10.016.
- [48] Z. Cheng, Z. Xu, S. Xu, X. Wang, Temperature dependent behavior of thermal conductivity of sub-5 Nm Ir film: defect-electron scattering quantified by residual thermal resistivity, J. Appl. Phys. 117 (2) (2015), 024307, https://doi.org/ 10.1062/1.4095607.
- [49] A. Nag, M.E.E. Alahi, S.C. Mukhopadhyay, Z. Liu, Multi-walled carbon nanotubes-based sensors for strain sensing applications, Sensors 21 (4) (2021) 1261, https://doi.org/10.3300/c21041261
- [50] D. Zhang, Z. Shao, D. Geng, X. Jiang, Y. Liu, Z. Zhou, S. Li, Feasibility study of wave-motion milling of carbon fiber reinforced plastic holes, Int. J. Extrem. Manuf. 3 (2021), 010401, https://doi.org/10.1088/2631-7990/abc675.
- [51] G. Eres, A.A. Puretzky, D.B. Geohegan, H. Cui, In situ control of the catalyst efficiency in chemical vapor deposition of vertically aligned carbon nanotubes on predeposited metal catalyst films, Appl. Phys. Lett. 84 (10) (2004) 1759–1761, https://doi.org/10.1063/1.1668325.
- [52] J.-C. Blancon, M. Paillet, H.N. Tran, X.T. Than, S.A. Guebrou, A. Ayari, A. San Miguel, N.-M. Phan, A.-A. Zahab, J.-L. Sauvajol, Direct measurement of the absolute absorption spectrum of individual semiconducting single-wall carbon nanotubes, Nat. Commun. 4 (1) (2013) 1–8, https://doi.org/10.1038/ pccmms3542
- [53] H. Zobeiri, R. Wang, C. Deng, Q. Zhang, X. Wang, Polarized Raman of nanoscale two-dimensional materials: combined optical and structural effects, J. Phys. Chem. C 123 (37) (2019) 23236–23245. https://doi.org/10.1021/acs.ipcc.9b06892.
- [54] J. Guo, X. Wang, T. Wang, Thermal characterization of microscale conductive and nonconductive wires using transient electrothermal technique, J. Appl. Phys. 101 (2007), 063537, https://doi.org/10.1063/1.2714679.
- [55] H. Lin, S. Xu, Y. Zhang, X. Wang, Electron transport and bulk-like behavior of Wiedemann-Franz law for sub-7 nm-Thin iridium films on silkworm silk, ACS Appl. Mater. Interfaces 6 (14) (2014) 11341–11347, https://doi.org/10.1021/ am501876d.

- [56] J. Liu, T.Y. Wang, S. Xu, P.Y. Yuan, X. Xu, X.W. Wang, Thermal conductivity of giant mono- to few-layered CVD Graphene supported on an organic substrate, Nanoscale 8 (19) (2016) 10298–10309, https://doi.org/10.1039/c6nr02258h.
- [57] Z. Cheng, M. Han, P. Yuan, S. Xu, B.A. Cola, X. Wang, Strongly anisotropic thermal and electrical conductivities of a self-assembled silver nanowire network, RSC Adv. 6 (93) (2016) 90674–90681, https://doi.org/10.1039/c6ra20331k.
- [58] X. Feng, X. Huang, X. Wang, Nonlinear effects in transient electrothermal characterization of anatase TiO<sub>2</sub> nanowires, Rev. Sci. Instrum. 83 (4) (2012), 044901, https://doi.org/10.1063/1.3702805.
- [59] Y. Xie, P. Yuan, T. Wang, N. Hashemi, X. Wang, Switch on the high thermal conductivity of graphene paper, Nanoscale 8 (40) (2016) 17581–17597, https:// doi.org/10.1039/c6nr06402g.
- [60] H. Fujishiro, T. Okamoto, K. Hirose, Thermal contact resistance between high-T-c superconductor and copper, Physica C 357 (2001) 785–788, https://doi.org/ 10.1016/S0921-4534(01)00364-1.
- [61] H. Lin, S. Xu, X.W. Wang, N. Mei, Significantly reduced thermal diffusivity of free-standing two-layer graphene in graphene foam, Nanotechnology 24 (41) (2013), 415706, https://doi.org/10.1088/0957-4484/24/41/415706.
- [62] Y.A. Yue, K. Liu, M. Li, X.J. Hu, Thermal manipulation of carbon nanotube fiber by mechanical stretching, Carbon 77 (2014) 973–979, https://doi.org/10.1016/j. carbon.2014.06.013.
- [63] C. Kittel. Introduction to Solid State Physics, seventh ed., Wiley, 1996.
- [64] Y. Xie, S. Xu, Z. Xu, H. Wu, C. Deng, X. Wang, Interface-mediated extremely low thermal conductivity of graphene aerogel, Carbon 98 (2016) 381–390, https://doi. org/10.1016/j.carbon.2015.11.033.
- [65] X.D. Tang, S. Xu, J.C. Zhang, X.W. Wang, Five orders of magnitude reduction in energy coupling across corrugated graphene/substrate interfaces, ACS Appl. Mater. Interfaces 6 (4) (2014) 2809–2818, https://doi.org/10.1021/am405388a.
- [66] G.H. Li, A. Luican, E.Y. Andrei, Scanning tunneling spectroscopy of graphene on graphite, Phys. Rev. Lett. 102 (17) (2009), 176804, https://doi.org/10.1103/ PhysRevLett.102.176804.
- [67] D. Yoon, Y.W. Son, H. Cheong, Negative thermal expansion coefficient of graphene measured by Raman spectroscopy, Nano Lett. 11 (8) (2011) 3227–3231, https://doi.org/10.1021/nl201488g.
- [68] N. Behabtu, C.C. Young, D.E. Tsentalovich, O. Kleinerman, X. Wang, A.W.K. Ma, E. A. Bengio, R.F. ter Waarbeek, J.J. de Jong, R.E. Hoogerwerf, S.B. Fairchild, J. B. Ferguson, B. Maruyama, J. Kono, Y. Talmon, Y. Cohen, M.J. Otto, M. Pasquali, Strong, light, multifunctional fibers of carbon nanotubes with ultrahigh conductivity, Science 339 (6116) (2013) 182–186, https://doi.org/10.1126/science.1228061.
- [69] Z. Cheng, L. Liu, S. Xu, M. Lu, X. Wang, Temperature dependence of electrical and thermal conduction in single silver nanowire, Sci. Rep. 5 (2015) 10718, https:// doi.org/10.1038/srep10718.
- [70] Y. Xie, M. Han, R. Wang, H. Zobeiri, X. Deng, P. Zhang, X. Wang, Graphene aerogel based bolometer for ultrasensitive sensing from ultraviolet to far-infrared, ACS Nano 13 (5) (2019) 5385–5396, https://doi.org/10.1021/acsnano.9b00031.
- [71] W. Desorbo, W.W. Tyler, The specific heat of graphite from 13-degrees-K to 300-degrees-K, J. Chem. Phys. 21 (10) (1953) 1660–1663, https://doi.org/10.1063/1.1698640.